Integrated induced-coherence spectroscopy in a single nonlinear waveguide

Pawan Kumar,* Sina Saravi, Thomas Pertsch, and Frank Setzpfandt
Institute of Applied Physics, Abbe Center of Photonics, Friedrich Schiller University Jena, Albert-Einstein-Strasse 15, 07745 Jena, Germany

(Received 23 December 2019; accepted 29 April 2020; published 29 May 2020)

We present a generalized understanding of the induced-coherence (IC) effect, aiming to find new strategies for engineering and optimizing the IC response of nonlinear systems. We establish that sensing the cross density of states (CDOS) of the field lies at the core of IC and that it is the spatial profile of the nonlinearity that determines how this CDOS information is sampled. Based on our findings, we identify integrated nonlinear waveguides as a versatile and suitable platform for spectroscopy based on IC and show that our generalized treatment allows us to optimize the sensing performance. Our results open the way for the design of compact IC-based spectroscopic devices with customized responses.

DOI: 10.1103/PhysRevA.101.053860

I. INTRODUCTION

Spontaneous parametric down-conversion (SPDC) enables the generation of signal and idler photon pairs from pump photons of shorter wavelength by a spontaneous nonlinear process. In general, signal photons from two coherently pumped sources do not show first-order interference, but this interference can be induced when the idler photons emitted from both sources are indistinguishable [1,2]. The interference contrast observed for the signal photons is directly linked to the indistinguishability of the idler photons, which also depends on the properties of the medium between the sources, through which the idler photons propagate. This effect is called induced coherence (IC) and can be used in a nonlinear interferometer [3] with two photon-pair sources to measure the idler-frequency transmission of objects placed in the idler path between the sources by detecting only the signal photons, as shown schematically in Fig. 1(a). The frequencies of signal (s) and idler (i) photons are anticorrelated, governed by the energy conservation law $\omega_p = \omega_i + \omega_s$, with the pump frequency ω_p. Thus, through the measurement of the signal spectral intensity alone, one can obtain spectral information about the objects in the idler photon path. Spectroscopic measurement techniques based on IC with strongly different signal and idler wavelengths are therefore particularly interesting to access technologically challenging spectral ranges like infrared and terahertz with detection only in the visible [4–12].

Most implementations of IC-based systems have used bulk nonlinear crystals, where generation and spectroscopy or imaging take place in sequence [3,13,14], similar to the scheme shown in Fig. 1(a). Here, IC is understood and treated in terms of changes to the photon operators associated with the plane-wave eigenmodes of the system at every stage [2,3,15,16], where the sensing process is separated from the SPDC. Alternatively, IC taking place during SPDC in a single continuous structure was used to sense the properties of the nonlinear system itself [5,10,11,17,18]. Here, IC is understood as the effect of the nonlinear system on the phase-matching condition, where the sensing happens during SPDC and cannot be separated from it. In general, it is not clear how a more complex and intertwined sequence of pair generation and IC sensing can take place, especially in structures with complex spatial distribution of linear and nonlinear susceptibilities or where photon operators cannot be defined, e.g., for intrinsically lossy or decaying modes [19].

Here, we develop a generalized understanding of IC that can be applied to any nonlinear system generating photon pairs, with the goal of finding new strategies in engineering and optimizing its response. We first identify a description of photon-pair generation capable of treating IC in arbitrary systems. Based on this, we explain the fundamental role of the cross density of states (CDOS) and the spatial profile of the nonlinearity in shaping the IC response and suggest nonlinear waveguides (WGs) as highly suitable platforms for engineering the IC response of a system, especially for spectroscopic applications. In WGs, the analyte to be sensed and measured modifies the CDOS when it interacts with the evanescent tails of the guided modes by introducing additional losses and changing the mode propagation constants. This in turn affects the IC response of the nonlinear WG. In particular, a change in the CDOS at a long idler wavelength influences the measured intensity at a short-wavelength signal generated through SPDC in the nonlinear WG. This effect was demonstrated in experimental results [17,18], for which, however, no rigorous analytical description exists to date. Using the generalized description of the IC effect, we will show that IC in waveguides can be used to extract both the real and imaginary parts of the wavelength-dependent refractive index of the analytes, thus realizing IC spectroscopy. Furthermore, we show that by engineering the nonlinearity of the WG, the performance of a spectroscopic device can be controlled and optimized. Using a well-designed and properly calibrated sensing system based on a nonlinear WG, IC could therefore be used to recognize specific substances based on their spectroscopic fingerprint and determine their concentrations.

*kpawan8791@gmail.com

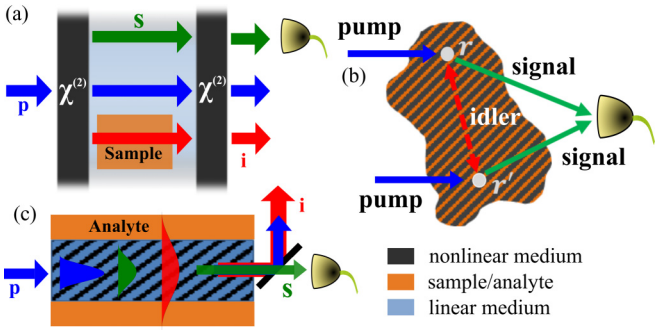

FIG. 1. (a) Sketch of induced coherence (IC) with two sequential photon-pair sources. (b) Schematic for the generalized description of IC based on Eq. (1). (c) Scheme for IC spectroscopy in a nonlinear waveguide. Pump, signal, and idler are denoted by p, s, and i, respectively. Different colors denote different materials, where striped regions indicate that several materials can be distributed inhomogeneously.

II. GENERALIZED DESCRIPTION OF IC

We describe IC rigorously using the Green's function (GF) quantization method [20], which has already been used to describe pair generation in nanostructured systems with complex dispersion and absorption properties [21–23]. In an IC experiment, the spectral or spatial dependence of the signal photon counts $W_s(\omega_s, \boldsymbol{r}_s, \hat{n})$ is measured, i.e., the detection rate of single photons with frequency ω_s at position $\boldsymbol{r}_s$ and polarized along the unit-vector direction $\hat{n} = \sum_\sigma n_\sigma \hat{\sigma}$, with $\sigma = \{x, y, z\}$. The idler photon is undetected, meaning that it is either absorbed or remains in the field. $W_s(\omega_s, \boldsymbol{r}_s, \hat{n})$ is [21]

$$W_s(\omega_s, \boldsymbol{r}_s, \hat{n}) \propto \sum n_\sigma n_{\sigma'} \iint d\boldsymbol{r}\, d\boldsymbol{r}'\, \Gamma_{\alpha\eta}(\boldsymbol{r})\Gamma^*_{\alpha'\eta'}(\boldsymbol{r}') \times \mathrm{Im}[G_{\eta\eta'}(\boldsymbol{r}, \boldsymbol{r}', \omega_i)] G_{\sigma\alpha}(\boldsymbol{r}_s, \boldsymbol{r}, \omega_s) \times G^*_{\sigma'\alpha'}(\boldsymbol{r}_s, \boldsymbol{r}', \omega_s), \quad (1)$$

where the sum is over indices σ, σ', α, η, α', and η'. Here, $\Gamma_{\alpha\eta}(\boldsymbol{r}) = \sum_\gamma \chi^{(2)}_{\alpha\eta\gamma}(\boldsymbol{r}) E_{p,\gamma}(\boldsymbol{r}, \omega_p)$ is the effective nonlinearity and includes the spatial profile of the material nonlinearity $\chi^{(2)}_{\alpha\eta\gamma}(\boldsymbol{r})$ and the complex-valued vectorial profile of the single-frequency pump beam $\boldsymbol{E}_p(\boldsymbol{r}, \omega_p)$. With a single-frequency pump, the idler frequency is fixed to $\omega_i = \omega_p - \omega_s$.

Based on this analytical description of the measured single-photon counts, we now develop a general understanding of the physics of IC. In Eq. (1), all the linear properties of the system are taken into account in the classical GF for the signal and idler frequencies. The information about the system at the idler frequency is carried by $\mathrm{Im}[G_{\eta\eta'}(\boldsymbol{r}, \boldsymbol{r}', \omega_i)]$, describing the CDOS $\rho(\boldsymbol{r}, \boldsymbol{r}', \omega_i)$ between the two points $\boldsymbol{r}$ and $\boldsymbol{r}'$[24] as

$$\rho(\boldsymbol{r}, \boldsymbol{r}', \omega_i) \propto \omega_i \mathrm{Im}[\mathrm{Tr} G_{\eta\eta'}(\boldsymbol{r}, \boldsymbol{r}', \omega_i)], \quad (2)$$

where Tr denotes the trace of the Green's tensor. The CDOS corresponds to the number of states connecting two points and is a measure of the spatial coherence between them [24]. The CDOS between each two points that can generate photon pairs is the fundamental system property at the idler frequency that is carried into the signal photon count rate through IC. The two GFs at the signal frequency describe the propagation of the signal radiation from $\boldsymbol{r}$ and $\boldsymbol{r}'$ to the signal detector, as schematically shown in Fig. 1(b). This happens for any pair of points in the system that possesses a nonlinearity and is taken into account by the volume integrals in Eq. (1), where the effective nonlinearity $\Gamma_{\alpha\eta}(\boldsymbol{r})$ determines how the CDOS is sampled. Hence, by shaping the effective nonlinearity, we can control how the system's CDOS at the idler frequency is imprinted on the signal photon properties.

We may better understand the phenomena of IC and its connection to the CDOS by considering a simplified one-dimensional system with coordinate z in which photon pairs can be generated only in very thin sections at the two ends of the system at positions z_1 and z_2, whereas the medium under test is between these sources. In this case $\Gamma(z, \omega_p) = \Gamma_1 \delta(z - z_1) + \Gamma_2 \delta(z - z_2)$. This configuration resembles most IC experiments [1–4,6]. The signal photon detection rate now becomes

$$W_s(\omega_s, z_s) \propto W_1 + W_2 + W_3, \quad (3)$$

where

$$W_{1/2} = \mathrm{Im}[G(z_{1/2}, z_{1/2}, \omega_i)] |\Gamma_{1/2} G(z_s, z_{1/2}, \omega_s)|^2, \quad (4)$$

$$W_3 = 2\,\mathrm{Im}[G(z_1, z_2, \omega_i)] \times \mathrm{Re}[\Gamma_1 \Gamma_2^* G(z_s, z_1, \omega_s) G^*(z_s, z_2, \omega_s)]. \quad (5)$$

W_1 and W_2 describe the individual responses of each of the sources and include $\mathrm{Im}[G(z_{1/2}, z_{1/2}, \omega_i)]$, the idler local density of states (LDOS) at each source. When all the waves are forward propagating, the LDOS is not affected by the medium between the sources, unless there is a reflection from the medium back into the source. Hence, the first two terms do not give any information about the medium between the sources. On the other hand, W_3 includes $\mathrm{Im}[G_i(z_1, z_2)]$, the CDOS between the two sources at the idler frequency. W_3 is affected by the medium between the two sources, whose properties contribute to the CDOS, and carries the information about it into the signal photon spectrum.

The influence of CDOS and the effective nonlinearity on IC can be used to engineer IC-based systems for optimized responses and potentially new functionalities in platforms that enable control over these parameters. Integrated WG platforms are a suitable candidate for this task, specifically for IC spectroscopy. They offer control over the CDOS through nanostructuring, either enhancing [25–27] or suppressing [22,28] pair generation. The effective nonlinearity in WGs can be controlled through the phase-matching condition, which can be tailored for shaping the biphoton state through periodic nanostructuring [29,30] or periodic poling in $\chi^{(2)}$ materials [31,32]. Moreover, IC in integrated WG platforms has already been demonstrated, either with two separated sources [33] or with one source during the generation stage [17,18]. Integrated WG platforms are already well established in linear optical sensing and spectroscopy [34–39], where the analyte is put in contact with the WG and the induced changes in its modal properties are probed through excitation and detection at the same wavelength. Hence, nonlinear WGs could be highly suitable for IC spectroscopy, offering compactness, controllability, stability, and cost-effectiveness. In the rest of this paper, we analytically and numerically describe and

investigate how IC spectroscopy can be performed in a single nonlinear WG. We also use our general understanding of IC to outline how a single WG can be engineered for an optimal realization of IC spectroscopy.

III. IC SPECTROSCOPY IN A SINGLE NONLINEAR WG

Our proposed scheme for IC spectroscopy in a single nonlinear WG is sketched in Fig. 1(c). Photon pairs are generated in the nonlinear core of the WG, exciting the guided signal and idler modes. Interaction with a potential analyte happens simultaneously through the evanescent tails of these modes, which can be designed so that only a long-wavelength idler mode interacts with the analyte (see Appendix D). Only the signal photons are detected. In the following, we present a general description of IC spectroscopy in a single nonlinear WG, regardless of its nonlinearity profile. We then analytically and numerically investigate two specific cases of nonlinearity profiles.

A. Analytical model

To describe IC in a single nonlinear WG, we use Eq. (1) in a scalar form for a one-dimensional (1D) system, with propagating modes along the z direction, which describes the main physics in this case. The information about the polarization dependence and the transverse spatial profile of the WG modes can be straightforwardly taken into account by using the full three-dimensional vectorial formula. We assume a 1D system with a z-invariant complex-valued dispersive refractive index $n(\omega)$ and with a potentially varying nonlinearity profile $\chi^{(2)}(z)$ that extends only from $z=0$ to $z=L$. The pump, signal, and idler modes of the WG are characterized by their complex-valued wave vectors β_p, β_s, and β_i, respectively, where $\beta(\omega)=\beta'+i\beta''=\frac{\omega n(\omega)}{c}$. In a 1D system, the rate at which signal photons are detected at the end of the WG is given by [22]

$$W_s(\omega_s,\omega_p,L)\propto\int_0^L dz\int_0^L dz'\Gamma(z,\omega_p)\Gamma^*(z',\omega_p)\times \mathrm{Im}[G(z,z',\omega_i)]G(L,z,\omega_s)G^*(L,z',\omega_s), \tag{6}$$

with $\Gamma(z,\omega_p)=\chi^{(2)}(z)E_p(z,\omega_p)$. $E_p(z,\omega_p)$ denotes the complex amplitude of the continuous-wave (cw) pump field at frequency ω_p. We take $E_p(z,\omega_p)=\exp(i\beta_p z)$, where we assume only a single pump mode is excited at the pump frequency. ω_s and $\omega_i=\omega_p-\omega_s$ are the frequencies of the signal and idler photons, respectively. The classical GF of the 1D system is given by [20]

$$G(z,z',\omega)=i\exp[i\beta(\omega)|z-z'|]/2\beta(\omega), \tag{7}$$

which fully describes the propagation of optical fields inside the medium in the presence of dispersion and linear losses. We insert this GF into Eq. (6) and after some straightforward calculations (see Appendix A) find

$$W_s(\omega_s,\omega_p,L)\propto\frac{\exp(-2\beta_s''L)}{8|\beta_s|^2|\beta_i|^2}\int_0^L dz\int_0^z dz'\times\chi^{(2)}(z)\chi^{(2)}(z')\mathrm{Re}[T_1(z,z')+T_2(z,z')], \tag{8}$$

with $T_1(z,z')$ and $T_2(z,z')$ given by

$$T_1(z,z')=\beta_i e^{i(\beta_p-\beta_s-\beta_i^*)z}e^{-i(\beta_p-\beta_s-\beta_i)^*z'}, \tag{9}$$

$$T_2(z,z')=\beta_i^* e^{i(\beta_p-\beta_s+\beta_i)z}e^{-i(\beta_p-\beta_s+\beta_i^*)^*z'}. \tag{10}$$

Equation (8), along with Eqs. (9) and (10), describes the rate of signal photon counts at the end of a single nonlinear WG. By looking at the wave-vector mismatch terms in Eqs. (9) and (10), it can be interpreted that T_1 and T_2 correspond to two different phase-matching processes that can result in the detection of a signal photon at the end of the structure. In both these processes the signal photon propagates in the forward z direction. However, in T_1 the idler photon is copropagating with the signal photon, while in T_2 it is counterpropagating with the signal photon in the backward direction. In general, both these processes would contribute to the final signal intensity detected at the end of the system, and their contributions are systematically accounted for in Eq. (8). In practice, only one of these phase-matching processes (usually the copropagating one) has a dominant contribution. This is determined by the spatial modulation of the nonlinearlity profile $\chi^{(2)}(z)$.

The signal spectral intensity function in Eq. (8) can account for the dispersion and losses of the pump, signal, and idler modes through their frequency-dependent complex-valued propagation constants. Furthermore, it encapsulates the spatial variation of the nonlinearity $\chi^{(2)}(z)$ in a general manner. Therefore, it can be used to analyze different variants of nonlinear interferometers, which may contain engineered $\chi^{(2)}(z)$ profiles. Here, we look at two specific cases. In the first design, the whole length of the WG is phase matched for a single copropagating pair-generation process. In the second design, we consider a case where two separated sections of the WG are phase matched for the same copropagating process.

B. WG with a homogeneous nonlinear section

We first consider the case of a single nonlinear WG of length L, phase matched for a single copropagating process. The process is phase matched all along the WG, where one way of achieving this is through periodically poling the nonlinearity profile of the WG. We refer to this case as having a homogeneous nonlinear section. We consider a case where the signal and pump do not interact with the analyte; hence, β_p and β_s are assumed to be real-valued quantities. The idler mode is assumed to be influenced by interaction with the external medium; hence, its propagation constant is complex valued, $\beta_i=\beta_i'+i\beta_i''$, where β_i'' accounts for the loss. In essence, we are considering a common WG source of photon pairs, in which only the idler mode is interacting with a potentially lossy analyte and we are detecting only the signal photon counts at the output, as sketched in Fig. 1(c).

Implementing these assumptions in Eq. (8) and after some simplifications (see Appendix B), we find the spectrum of the signal single-photon counts has the following simple form:

$$W_s(\omega_s)\propto 2\mathrm{Re}[(1+i\Delta\beta L-e^{i\Delta\beta L})/(\Delta\beta)^2], \tag{11}$$

where $\Delta\beta=(\beta_p-\beta_s-\beta_i'-K)+i\beta_i''$ is the complex phase mismatch. Here, $2\pi/K$ is the period of periodic poling of nonlinearity $\chi^{(2)}(z)$, which is potentially needed to reach phase matching. The proportionality factor in Eq. (11) is

chosen such that for the case of a lossless idler mode, $\beta_i'' = 0$, it produces the well-known sinc-shaped spectral function $\mathrm{sinc}^2(\Delta\beta L/2)L^2$. Equation (11) shows that IC in a WG system is mainly controlled by $\Delta\beta$ and is shaped by the interference of photon pairs generated at different positions. The CDOS at the idler frequency between different points of generation depends on the complex wave vector of the idler mode, and it is this information that is carried to the signal photon spectra via $\Delta\beta$. In the following, we show, using a numerical example, how this configuration can be used to gain information about the properties of the idler mode.

For our numerical implementation, we consider a high-index-contrast ridge WG in lithium niobate [40] (see Appendix D) with a length of $L = 1$ mm, where phase matching is achieved by periodic poling, although modal phase matching without poling is also a possibility in these structures [40]. We choose the poling period such that a cw pump laser at $\lambda_p \approx 662$ nm wavelength is phase matched to the signal mode at $\lambda_s \approx 900$ nm and the idler mode at $\lambda_i \approx 2500$ nm wavelength, where we want to probe the optical properties. In our example these three optical modes are the fundamental quasi-TM modes of the WG. In implementations of IC spectroscopy using bulk optical components such as nonlinear crystals, the pump is commonly fixed to a single-frequency, and the angular and spectral distribution of the signal photons is collected to gain information about the idler [3]. In a 1D WG system, the angular degree of freedom does not exist. However, the dispersion of the optical modes of the WG, specifically at the pump and signal frequency, can be utilized to gain a degree of freedom in WG-based realization of IC spectroscopy. This is illustrated through the numerical example we provide here, where we use the pump frequency as an extra degree of freedom to show that IC in single WGs can be used for spectroscopic measurements.

We assume a spectrally localized loss induced in the idler mode by the analyte, described by $\beta_i'' = \gamma_i \times e^{-[(\lambda_i-\bar{\lambda})/\Delta\lambda]^2}$, with central wavelength $\bar{\lambda} = 2500$ nm, width $\Delta\lambda = 15$ nm, and magnitude γ_i. Figure 2(a) shows the signal spectrum $W_s(\omega_s)$ for different pump wavelengths. Clearly, the spectrally localized idler loss induces a dip in the signal intensity. In Fig. 2(b), we plot the signal intensity for $\lambda_p = 661.76$ nm, indicated by the red dashed line in Fig. 2(a). At this pump wavelength, the center of the phase-matching curve coincides with the center of the idler absorption line. The corresponding signal spectrum is shown for three idler loss magnitudes, $\gamma_i L = 0, 2, 4$ (blue, red, and green curves). Modification of the signal spectral intensity due to the idler loss is evident, as it shows a dip in its intensity. The central wavelength and width of this dip correspond to the idler absorption line, through which the loss spectrum can be derived from Eq. (11).

The proposed IC spectroscopy scheme in a single WG can measure changes in β_i'' and β_i', as both quantities influence the CDOS. However, extracting both simultaneously for a specific idler wavelength λ_i^* is not possible from the spectrum shown in Fig. 2(b), as only a single point corresponds to that specific idler wavelength, which cannot uniquely determine two quantities. To enable this, a signal spectrum with a pump wavelength constrained by $\lambda_p^{-1} = \lambda_s^{-1} + (\lambda_i^*)^{-1}$ should be obtained, which corresponds to a fixed λ_i^*. An example

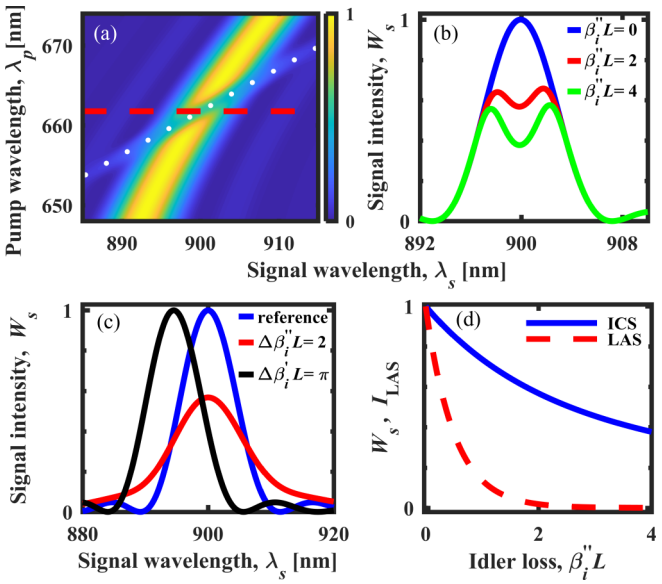

FIG. 2. (a) Normalized signal spectral intensity $W_s(\omega_s)$ from Eq. (11) for a single WG in the presence of an idler loss spectrally localized around $\lambda_i = 2500$ nm as a function of different cw pump wavelengths. (b) Signal intensity with a cw pump at $\lambda_p = 661.76$ nm for different idler loss magnitudes. (c) Signal intensity for a fixed idler wavelength $\lambda_i = 2500$ nm. For each λ_s, λ_p is varied to correspond to the fixed λ_i. (d) Comparison of single-WG IC spectroscopy (ICS) with linear absorption sensing or spectroscopy (LAS).

for $\lambda_i^* = 2500$ nm is indicated by the white dotted line in Fig. 2(a). The signal spectrum along this line is displayed in Fig. 2(c) for a lossless reference WG ($\Delta\beta_i'' = \Delta\beta_i' = 0$, blue), a WG with loss ($\Delta\beta_i'' L = 2$, $\Delta\beta_i' = 0$, red), and a WG with changed idler propagation constant ($\Delta\beta_i'' = 0$, $\Delta\beta_i' L = \pi$, black). Clearly, the signal spectrum for the WG with idler loss shows reduced fringe visibility; its maximum is reduced together with the increase in its minima. This behavior is similar to IC spectroscopy using bulk crystals [6] and can be attributed to imperfect IC due to idler loss [2]. A change in the real part of the propagation constant spectrally shifts the interference pattern. In general, both $\Delta\beta_i'$ and $\Delta\beta_i''$ for a specific idler wavelength could be nonzero and can be extracted from the signal spectra collected by varying the pump wavelength.

In Fig. 2(d) we compare the normalized signal intensity measured in IC spectroscopy at 900 nm with the transmitted intensity at 2500 nm that would be measured in linear absorption spectroscopy for increasing loss. Whereas in linear spectroscopy the intensity decreases exponentially, the IC signal has a slower decay. This indicates a larger sensitivity for linear spectroscopy compared to IC spectroscopy. On the other hand, the signal in linear spectroscopy becomes increasingly smaller than the one in IC spectroscopy, leading to a more challenging detection. Hence, IC spectroscopy in principle could offer a larger dynamic range.

To investigate the length and loss-dependent properties of IC spectroscopy in the limits of large and small idler losses, we examine the signal intensity function in Eq. (11) in more detail. Under the condition of exact phase matching

$\mathrm{Re}(\Delta\beta) = 0$, it can be expressed as

$$W_s(\beta_i'') \propto 2\left\{\frac{\exp(-\beta_i'' L) + \beta_i'' L - 1}{(\beta_i'')^2}\right\} = \left[1 - \frac{(\beta_i'' L)}{3} + \frac{(\beta_i'' L)^2}{12} + \cdots\right] L^2, \quad (12)$$

where W_s is Taylor expanded in the normalized idler loss $\beta_i'' L$. It can be noted that Eq. (12) produces the quadratic dependence of the signal intensity on the length, $W_s(\beta_i'' = 0) \propto L^2$, for a lossless idler. Such a dependence originates from the perfect induced coherence in the structure in this case, which allows the coherent addition of signal photon amplitudes produced in the elemental photon-pair sources that constitute the extended source of length L. However, the induced coherence is reduced when the idler mode experiences loss, and the resulting signal intensity is affected. In particular, for small losses $W_s(\beta_i'') \approx [1 - (\beta_i'' L)/3] W_s(\beta_i'' = 0)$, which reveals that the decrease in signal intensity due to small idler losses in the first order is simply proportional to $\beta_i'' L/3$, where we have neglected the higher-order terms in the Taylor expansion. This characteristic dependence of $W_s(\beta_i'')$ on the length of the WG explains why linear absorption spectroscopy is more sensitive than IC spectroscopy at small losses. For linear spectroscopy, the transmitted intensity would be given by $I(\beta_i'') = e^{-2\beta_i'' L} I(\beta_i'' = 0)$, which for low losses can be approximated as $I(\beta_i'') \approx [1 - 2\beta_i'' L] I(\beta_i'' = 0)$. Therefore, the decrease in intensity for linear spectroscopy is faster than the decrease in the signal intensity for IC spectroscopy in the regime of low idler losses. The origin of the particular length dependence of $W_s(\beta_i'')$, namely, its decrease being proportional to $L/3$, can be understood by noting that the decrease in signal intensity arises from reduced coherence due to the idler loss and not from the absorption of the signal intensity itself. One would therefore expect the length dependence of $W_s(\beta_i'')$ to reflect the dependence of average coherence on the length of the WG. Since the WG can be thought of as being composed of elemental photon-pair sources of infinitesimal length, the extent of the reduction in average coherence for the whole WG is determined by the average separation between a pair of these elemental sources, which is smaller than the total length of the WG; in particular it is $L/3$ for a homogeneous waveguide. This explains the slow decrease of signal intensity with idler loss compared to linear spectroscopy as long as the losses are small. On the other hand, in the limit of large losses ($\beta_i'' L \gg 1$) it is easy to see from Eq. (12) that $W_s(\beta_i'') \propto 2L/\beta_i''$. In this case the signal intensity increases linearly with the length of the WG because the signal amplitudes from individual elemental sources in the WG add up incoherently as the induced coherence between any pair of these elemental sources is negligibly small. At the same time, if we compare the behavior of IC spectroscopy with linear absorption spectroscopy at large losses, we find that signal intensity for IC spectroscopy decreases inversely with β_i'', while the intensity in linear spectroscopy decreases exponentially. This explains why IC spectroscopy can work better at large idler losses than linear absorption spectroscopy. This is simply because linear spectroscopy is characterized by an exponential decrease of the signal with increasing loss, whereas in IC spectroscopy the signal intensity decreases more slowly with increasing losses so its detection can be less challenging.

C. WG with two separated nonlinear sections

After analyzing IC spectroscopy in a homogeneous nonlinear WG, in this section we show how the response can be engineered through the spatial profile of the effective nonlinearity, which can be changed by using an inhomogeneous poling profile. This does not change the CDOS but changes how it is sampled along the WG. We consider a structure where two sections of the WG of length l are similarly poled to have $\Delta\beta \approx 0$ for a copropagating process for the wavelengths of interest. Between these sections exists a central section of length $L - 2l$, which is not poled and hence not phase matched and therefore acts effectively as a linear WG connecting two photon-pair sources of length l. The analyte is distributed along the complete length of the WG as in the homogeneous case discussed before. This geometry resembles closely the common implementation of nonlinear interferometers using two separated bulk sources [3], except for the fact that the analyte is assumed to be distributed homogeneously along the complete length of the interferometer instead of being present only in the region between the two sources. We find the signal intensity $W_s(\omega_s)$ analytically for this scenario (see Appendix C):

$$W_s(\omega_s) \propto 2\mathrm{Re}\left[2\left\{\frac{1 + i\Delta\beta l - e^{i\Delta\beta l}}{(\Delta\beta)^2}\right\} + e^{i\Delta\beta(L-l)}\left\{\frac{2 - e^{i\Delta\beta l} - e^{-i\Delta\beta l}}{(\Delta\beta)^2}\right\}\right]. \quad (13)$$

The two terms contributing to the signal intensity in Eq. (13) have different origins. While the first term can be identified as the contribution originating from each nonlinear section individually and hence is identical to the signal intensity expression for a single source given by Eq. (11), the second term reflects the interference between two-photon amplitudes arising from different nonlinear sections.

Like for the homogeneous single-source design case, we inspect the behavior of the signal intensity W_s by considering Eq. (13) under the phase-matching condition $\mathrm{Re}(\Delta\beta) = 0$. Here, we assume a case where at phase matching the outputs from two sources interfere constructively to produce the largest signal intensity. Taylor expanding $W_s(\beta_i'')$ around $\beta_i'' = 0$ results in $W_s(\beta_i'') \propto [1 - \beta_i''(3L - 2l)/6 + \cdots](2l)^2$. Therefore, for small idler loss $\beta_i'' L \ll 1$, the decrease in signal intensity is characterized by the length $(3L - 2l)/6$, which is, like in the homogeneous single-source design case, the average separation between two elemental photon-pair sources constituting the interferometer. On the other hand, in the limit of large idler loss the induced coherence becomes negligible, and the resulting signal intensity simply becomes $W_s(\beta_i'') \propto 4l/\beta_i''$. This linear dependence on the length l of the nonlinear section reflects the incoherent nature of signal intensity generation in the WG interferometer at large idler loss.

We plot W_s for different pump wavelengths in Fig. 3(a) for a geometry with total length $L = 2.8$ mm and sources of length $l = 0.5$ mm. Now, the spectra show densely spaced

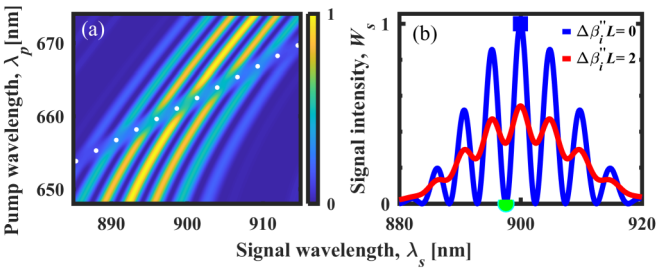

FIG. 3. (a) Normalized signal intensity $W_s(\omega_s)$ for a single WG with two phase-matched sections separated by a non-phase-matched one. (b) Signal intensity for a fixed idler wavelength of λ_i^*=2500 nm for the lossless and lossy idlers.

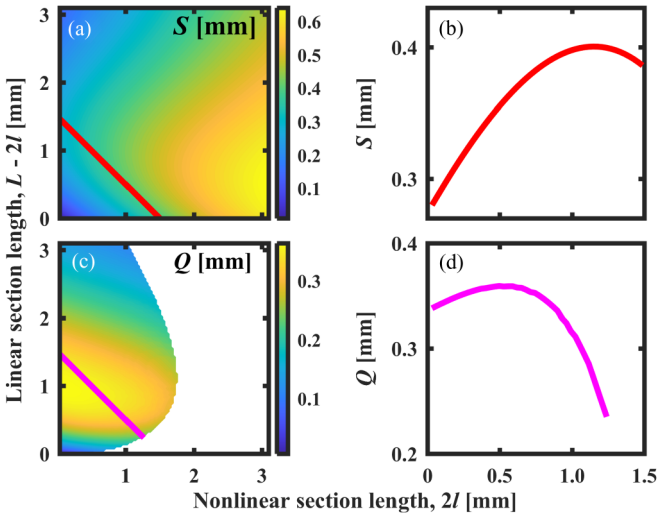

FIG. 4. Sensitivity of IC spectroscopy using WG configurations with varying lengths of the linear section $L - 2l$ and the nonlinear sections $2l$ in the presence of fixed idler loss $\beta_i'' = 1\ \mathrm{mm}^{-1}$. (a) The intensity sensitivity S and (b) a cut through it for a constant total length $L = 1.5$ mm. (c) and (d) Similar data for the visibility sensitivity Q.

fringes caused by the interference between the separated source sections. Such fringes have been observed in the angular domain for separated bulk sources [6,7]. The interferences within the two equal sources determine the fringe envelope, similar to what occurs for homogeneous nonlinear WGs. Again, losses at the longer idler wavelength modify the signal interference pattern. A cut through Fig. 3(a) along the dotted white line corresponding to a fixed idler wavelength of $\lambda_i^* = 2500$ nm is shown in Fig. 3(b) for a lossy case and the lossless case. Addition of loss results in an increase of the minima in the interference pattern and a reduction of the interference visibility, as described in the original IC experiment [1].

Controlling the effective nonlinearity to influence how the tested system properties manifest in the measured signal enables optimization of the measurement device. Here, we investigate the sensitivity of IC spectroscopy in WGs for varying lengths of the linear section $L - 2l$, where $L = 2l$ results in the configuration with homogeneous nonlinearity. We consider two measurement schemes. The sensitivity of intensity measurements at a single wavelength in one of the maxima is defined as $S = \frac{1}{W_s(\beta_i'')} \frac{\partial W_s}{\partial \beta_i''}$. Alternatively, the loss can be determined by measuring the visibility $V = (W_s^{\max} - W_s^{\min})/(W_s^{\max} + W_s^{\min})$ using the adjacent peak (marked by the blue square) and minimum (marked by the green circle) signal intensities, as shown in Fig. 3(b). In contrast to intensity measurements, the visibility measurement can reveal the absolute value of loss at a single idler wavelength without prior calibration as it is independent of the nonlinear conversion efficiency. The sensitivity of such a measurement is defined as $Q = \frac{\partial V}{\partial \beta_i''}$. The intensity and the visibility sensitivities for a fixed idler loss of $\beta_i'' = 1\ \mathrm{mm}^{-1}$ depending on the lengths of linear and nonlinear sections are shown in Figs. 4(a) and 4(c), respectively. The white region in Fig. 4(c) corresponds to a parameter range where visibilities cannot be defined as the spectral minima vanish.

Increasing the length of the nonlinear sections $2l$ always increases the intensity sensitivity in Fig. 4(a), whereas the visibility sensitivity in Fig. 4(c) decreases for $L - 2l \geqslant \beta_i''^{-1}$. For a fixed length of the nonlinear sections $2l$, there exists an optimal length of the linear section $L - 2l$ between the sources for maximizing the sensitivity, which for the S measurement is zero if $2l \gg \beta_i''^{-1}$. Here, the configuration with homogeneous nonlinearity becomes optimal. For fixed total length of the structure, an optimum combination of the linear and nonlinear sections that maximizes the sensitivity exists for both measurements. This can be seen in Figs. 4(b) and 4(d), where S and Q are plotted for a constant total structure length of $L = 1.5$ mm as a function of the total length of the nonlinear sections, $2l$. Hence, the type of measurement has a defining effect on the optimal configuration. Nonetheless, the theoretical formulation combined with our presented analysis provides a systematic way to identify the optimum configuration for IC spectroscopy in WGs.

Our discussion of the visibility of the signal interference and its dependence on the idler loss up to now assumed that the loss in the pump and signal modes is zero. However, in practical realizations of IC spectroscopy, finite losses will always be present at these spectral components due to either waveguide imperfections, absorption in the waveguide material, or absorption due to weak interaction with the analyte. We analyzed the sensitivity of the effects discussed before (see the detailed discussion in Appendix E) and found that for moderate signal or pump losses the visibilities will not notably change. Interestingly, if signal and pump losses are equal, the interference visibility will always remain the same, regardless of their magnitude. A similar loss-matching condition has been discussed in the context of biphoton spectral correlations in SPDC [41,42].

IV. CONCLUSION

In this work, we presented a generalized analysis of the IC effect, demonstrating the fundamental role of the CDOS and nonlinearity profile in controlling IC. From this understanding, we proposed the use of integrated nonlinear WGs as suitable platforms for performing IC spectroscopy. Through analytical formulations and numerical investigations of a realistic WG system, we showed how IC spectroscopy can be performed and also engineered for an optimized response. Our

work establishes the potential of nonlinear WGs as compact and controllable platforms for performing IC spectroscopy, especially for the infrared range. Our analysis also opens the way for the design of more complex IC-based systems, e.g., by using periodically nanostructured WGs, which provide an even stronger control over the density of states and the phase-matching condition compared to ridge WGs.

ACKNOWLEDGMENTS

P.K. acknowledges support from the Carl Zeiss Foundation. This work was funded by the German Federal Ministry of Education and Research (13N14877), the German Research Foundation (SE 2749/1-1), and the Free State of Thuringia (2017 FGR 0067, 2017 IZN 0012) using funding from the European Social Funds and the European Funds for Regional Development.

APPENDIX A: STEPS IN DERIVING EQUATION (8) FOR SIGNAL PHOTON DETECTION RATE IN A 1D WG

Here, we show how the result in Eq. (8) is derived starting from Eq. (6). By looking at the structure of the GF in Eq. (7), it can be easily verified that the integrand $I(z,z')$ in Eq. (6) satisfies $I(z,z') = I^*(z',z)$. We can use this fact to let go of the absolute value expression in the GF formula to allow for a simpler integration of the expression. We have

$$\begin{aligned} W_s &\propto \int_0^L dz \int_0^z dz' I(z,z') + \int_0^L dz \int_z^L dz' I(z,z') \\ &= \int_0^L dz \int_0^z dz' I(z,z') + \int_0^L dz' \int_{z'}^L dz I(z',z) \\ &= \int_0^L dz \int_0^z dz' I(z,z') + \int_0^L dz' \int_{z'}^L dz I^*(z,z'). \end{aligned}$$

The two integrals in the last equation have equivalent integration ranges. Consequently, we can restrict the range of integration such that $L \geqslant z \geqslant z' \geqslant 0$ and $W_s = \int_0^L dz \int_0^z dz' I(z,z') + \text{c.c.} = 2\text{Re}[\int_0^L dz \int_0^z dz' I(z,z')]$. In this integration range, we can put $|z-z'| = z-z'$, $|L-z'| = L-z'$, and $|L-z| = L-z$ in the GF expressions appearing in Eq. (6). Using this and inserting the expressions for the GFs and the pump field into Eq. (6), we find the following expression:

$$\begin{aligned} &W_s(\omega_s,\omega_p,L) \\ &\propto \frac{\exp(-2\beta_s'' L)}{8|\beta_s|^2|\beta_i|^2}\text{Re}\Bigg[\int_0^L dz \int_0^z dz' \\ &\quad \times \chi^{(2)}(z)\chi^{(2)}(z')\exp\{i(\beta_p-\beta_s)z\}\exp\{-i(\beta_p-\beta_s)^* z'\} \\ &\quad \times \left[\beta_i^* \exp\{i\beta_i(z-z')\} + \beta_i \exp\{-i\beta_i^*(z-z')\}\right]\Bigg]. \end{aligned} \tag{A1}$$

Rearranging the terms in this equation bring us to Eq. (8).

APPENDIX B: STEPS IN DERIVING EQUATION (11) FOR A WG WITH A HOMOGENEOUS NONLINEAR SECTION

Here, we show how Eq. (11) is derived from the more general Eq. (8) for the special case of a WG with a homogeneous nonlinear section. For this, we assume the following spatial profile of the nonlinearity:

$$\begin{aligned} \chi^{(2)}(z) &= \sin(Kz)\text{rect}\left(\frac{z-\frac{L}{2}}{L}\right) \\ &= \frac{[\exp\{iKz\} - \exp\{-iKz\}]}{2i}\text{rect}\left(\frac{z-\frac{L}{2}}{L}\right). \end{aligned} \tag{B1}$$

This is a periodic profile of period $2\pi/K$, which is restricted only to the range between zero and L by the rectangular function. Such a $\chi^{(2)}(z)$ profile is realized in practice through periodic poling of the nonlinear media where periodic modulation of homogeneous $\chi^{(2)}$ produces several Fourier components. Out of these, a single Fourier component, here denoted by the wave vector K, is usually employed to achieve quasiphase matching for the down-conversion process. We assume that this Fourier component results in satisfying the copropagating phase-matching condition; hence, we keep only the contribution from the term $T_1(z,z')$ in Eq. (8). Furthermore, the propagation constants $|\beta_s|$ and $|\beta_i|$ usually do not vary drastically over the bandwidth of the down-conversion. So the spectral variations in the amplitude of the factor $\frac{1}{|\beta_s|^2|\beta_i|^2}$ can be neglected. Finally, it is reasonable to assume that $\beta_i' \gg \beta_i''$ and hence the approximation $\frac{\beta_i}{|\beta_i|} \approx 1$ can be made, so that the spectral variations of β_i appearing as a factor in the amplitude of T_1 can be neglected. It should be noted that if we are in a highly dispersive regime of material properties that strongly varies these propagation constants, these approximations are not valid, and the more general formula in Eq. (8) must be used. Using the above approximation in Eq. (8), we arrive at

$$\begin{aligned} W_s(\omega_s,\omega_p,L) \propto 8e^{-2\beta_s'' L}\,\text{Re}\Bigg[&\int_0^L dz \int_0^z dz' \chi^{(2)}(z) \\ &\times \chi^{(2)}(z') e^{i(\beta_p-\beta_s-\beta_i^*)z} e^{-i(\beta_p-\beta_s-\beta_i)^* z'}\Bigg]. \end{aligned} \tag{B2}$$

We have included the factor of 8 here so that the final result for a lossless and phase-matched structure of length L becomes L^2, as will be seen in the following.

Inserting the nonlinearity profile of Eq. (B1) into Eq. (B2) leads to four terms which correspond to the four exponential terms in the product $\chi^{(2)}(z)\chi^{*(2)}(z') = \frac{1}{4}[\exp(iKz) - \exp(-iKz)][\exp(-iKz') - \exp(iKz')]$, where $0 \leqslant z, z' \leqslant L$. We keep only a single term out of these four which corresponds to phase-matched SPDC. Effectively, we substitute $\chi^{(2)}(z)\chi^{*(2)}(z')$ by $\frac{1}{4}\exp(-iKz)\exp(iKz')$ in Eq. (B2), and this leads to

$$\begin{aligned} \frac{W_s(\omega_s,\omega_p,L)}{2e^{-2\beta_s'' L}} &\propto \text{Re}\left[\int_0^L dz \int_0^z dz' e^{ipz} e^{-iqz'}\right] \\ &= \text{Re}\left[\frac{1}{q}\left\{\left(\frac{e^{i(p-q)L}-1}{p-q}\right) - \left(\frac{e^{ipL}-1}{p}\right)\right\}\right], \end{aligned} \tag{B3}$$

with p and q defined as $p = \beta_p - \beta_s - \beta_i^* - K$ and $q = \beta_p^* - \beta_s^* - \beta_i^* - K$. Considering lossless pump and signal modes, $\beta_p'' = \beta_s'' = 0$, and a lossy idler mode, we have $p = q = \Delta\beta =$

$(\beta_p - \beta_s - \beta_i' - K) + i\beta_i''$. In this case $\frac{\exp\{i(p-q)L\}-1}{p-q} \to iL$, and we get Eq. (11) as the result.

APPENDIX C: STEPS IN DERIVING EQUATION (13) FOR A WG WITH TWO SEPARATED NONLINEAR SECTIONS

Here, we show how Eq. (13) is derived from the more general Eq. (8) for the special case of a WG with two separated nonlinear sections. We consider a structure consisting of two nonlinear sections, each of length l, in which the structure is periodically poled and hence phase matched. We consider a case where both nonlinear sections are poled similarly and phase matched for the same copropagating process. The whole WG has the length L, and there is an unpoled section of length $L - 2l$ between the two poled sections. Since the phase matching is not satisfied in this region, we take it to be effectively linear. The effective $\chi^{(2)}(z)$ for such a system can be modeled as

$$\chi^{(2)}(z) = \sin(Kz)\,\mathrm{rect}\left[\left(z - \frac{l}{2}\right)\Big/ l\right] + \sin\{K[z-(L-l)]\}\,\mathrm{rect}\left\{\left[z - \left(L - \frac{l}{2}\right)\right]\Big/ l\right\}. \tag{C1}$$

The signal spectral function for this case can be calculated in a manner analogous to the homogeneous nonlinear section case by inserting the $\chi^{(2)}(z)$ profile from Eq. (C1) into Eq. (8) and keeping only the terms dominant through the phase-matching condition. Such a calculation gives $W_s \propto 8\exp(-2\beta_s'' L)\mathrm{Re}[F_1 + F_2 + F_3]$, where

$$\begin{aligned}
F_1 &= \int_0^l dz \int_0^z dz' \sin(Kz)\sin(Kz') e^{i(\beta_p-\beta_s-\beta_i^*)z} e^{-i(\beta_p-\beta_s-\beta_i)^* z'} \approx \frac{1}{4}\int_0^l dz \int_0^z dz' e^{ipz} e^{-iqz'},\\
F_2 &= \int_{L-l}^L dz \int_0^l dz' \sin\{K[z-(L-l)]\}\sin(Kz') e^{i(\beta_p-\beta_s-\beta_i^*)z} e^{-i(\beta_p-\beta_s-\beta_i)^* z'}\\
&\approx \frac{1}{4} e^{i(\beta_p-\beta_s-\beta_i^*)(L-l)} \int_0^l dz \int_0^l dz' e^{ipz} e^{-iqz'},\\
F_3 &= \int_{L-l}^L dz \int_{L-l}^z dz' \sin\{K[z-(L-l)]\}\sin\{K[z'-(L-l)]\} e^{i(\beta_p-\beta_s-\beta_i^*)z} e^{-i(\beta_p-\beta_s-\beta_i)^* z'}\\
&\approx \frac{1}{4} e^{-2(\beta_p''-\beta_s'')(L-l)} \int_0^l dz \int_0^z dz' e^{ipz} e^{-iqz'},
\end{aligned} \tag{C2}$$

with p and q defined as before. We note that contributions F_1 and F_3 to the total signal intensity are similar to the intensity expression given in Eq. (B3). They originate from the first and second nonlinear sections, respectively, and can be thought of as coming from the interference of signal amplitudes from within these two sources separately. The sum of these terms therefore represents the incoherent addition of signal intensity from these sources. The remaining term, F_2, results from the interference of signal amplitude produced in the first source with that from the second source. If the pump and signal modes are lossless, $F_1 = F_3$, and thus, $W_s \propto 8\mathrm{Re}[2F_1 + F_2]$. Explicitly,

$$W_s(\omega_s, \omega_p, L) \propto 2\mathrm{Re}\left[2\left\{\frac{1 + i\Delta\beta l - e^{i\Delta\beta l}}{(\Delta\beta)^2}\right\} + e^{i(\Delta\beta+K)(L-l)}\left\{\frac{2 - e^{i\Delta\beta l} - e^{-i\Delta\beta l}}{(\Delta\beta)^2}\right\}\right], \tag{C3}$$

with wave-vector mismatch $\Delta\beta$ defined as before. We can use the expression in Eq. (C3) and calculate signal intensity in the limit of vanishing wave-vector mismatch, $\Delta\beta = 0$, to be $W_s \propto 2l^2[1 + \cos\{K(L-l)\}]$. This clearly illustrates the interferometric nature of the two-source design. Depending on the value of the phase $K(L-l)$, the signal amplitude from the first source interferes constructively or destructively with the signal amplitude generated in the second source. We restrict the choice of lengths in our designs such that $K(L-l) = m2\pi$, with $m \in \mathbb{N}$. This ensures that interference is constructive when wave-vector mismatch is zero and results in the maximum of the interference fringes coinciding with the maximum of the phase-matching spectrum, as can be seen in Fig. 3(b). It is for this reason that K does not appear explicitly in the signal intensity expression in Eq. (13).

A case of particular interest is when the nonlinear length l is small enough that the approximation $|\Delta\beta l| \ll \pi$ is valid while $\Delta\beta L$ is non-negligible. This would be applicable for interferometers employing broadband sources of photon pairs. Under this condition,

$$W_s \propto 2l^2\{1 + \exp(-\beta_i'' L)\cos(\mathrm{Re}[\Delta\beta]L)\}. \tag{C4}$$

Essentially, in arriving at Eq. (C4) we have assumed that the losses in the two nonlinear sources that generate the photon pair are negligible and thus the signal intensity generated by any one of them alone is proportional to l^2. However, the linear medium separating the two sources has losses, and thus, the interference of signal amplitudes generated by these two sources can get washed out. We note that Eq. (C4) describes nonlinear interferometers where the losses are present exclusively in the linear region between the sources, with sources themselves being lossless.

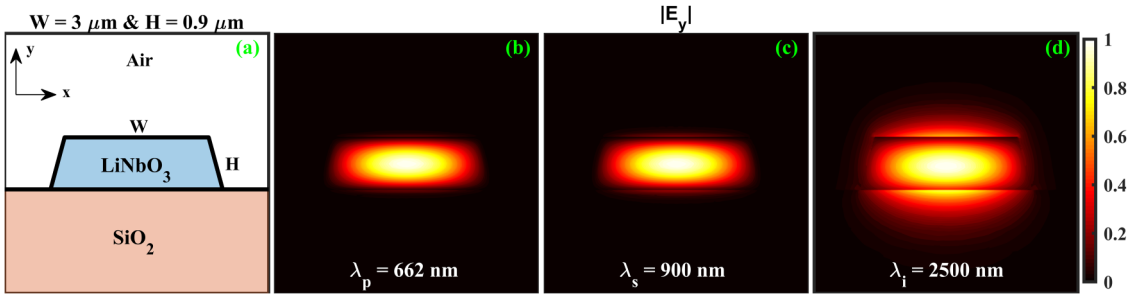

FIG. 5. Waveguide design for investigating proposed induced-coherence spectroscopy. (a) Design for ridge waveguide in a z-cut $LiNbO_3$ on an insulator sample. Considered (b) pump, (c) signal, and (d) idler fundamental quasi-TM modes of the waveguide.

APPENDIX D: WAVEGUIDE DESIGN FOR INDUCED COHERENCE SPECTROSCOPY

We propose to use a high-index contrast ridge waveguide in lithium niobate ($LiNbO_3$) to implement the concept of infrared spectroscopy based on induced coherence in down-conversion in the nonlinear waveguide. The waveguide design that we consider to demonstrate this is shown in Fig. 5(a). It is similar to the waveguides demonstrated recently in $LiNbO_3$ on an insulator platform [40,43,44]. Here, we assume a z-cut $LiNbO_3$ sample such that the c axis of the crystal lies along the y axis shown in the figure. Such a configuration can allow making use of the largest second-order susceptibility element, d_{33}, of $LiNbO_3$ by making use of the quasi-TM modes of the waveguide. We calculate the effective index of the fundamental TM modes for this structure using COMSOL MULTIPHYSICS (shown in Fig. 6). In the plot we have marked the wavelengths and corresponding effective indices for the pump (p), signal (s), and idler (i) modes considered for performing the calculations in this work. The corresponding mode profiles are shown in Figs. 5(b), 5(c) and 5(d), respectively. It can be noted that the pump and signal modes are confined within the waveguide due to their smaller wavelengths compared to the dimensions of the waveguide. On the other hand, the longer wavelength idler mode can be noted to have a long evanescent tail that appreciably extends outside the waveguide into the air above it. This feature can be controlled by appropriately designing the waveguide so that the idler mode can be used to sense the medium above the waveguide, as proposed here. We mention that to realize quasiphase-matched down-conversion in the waveguide using fundamental TM-like modes, the waveguide needs to be periodically poled with a period of 4.61 μm. Such periodically poled waveguide structures with comparable poling periods were recently demonstrated in ridge $LiNbO_3$ waveguides [44].

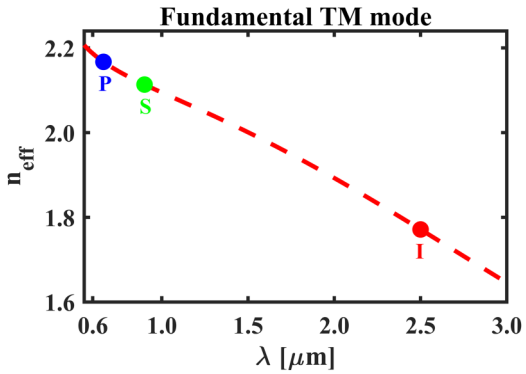

FIG. 6. Effective index n_{eff} of the fundamental quasi-TM mode of the waveguide shown in Fig. 5(a) as a function of wavelength.

APPENDIX E: EFFECT OF PUMP AND SIGNAL LOSSES ON INDUCED COHERENCE SPECTROSCOPY OF THE IDLER

So far, we have restricted ourselves to the discussion of induced coherence under lossless pump and signal modes. Although we showed in Appendix D how a judicious design of the waveguides for implementing integrated IC spectroscopy can minimize the interaction of the pump and signal modes with the analytes surrounding these waveguides, it is nevertheless important to consider the effects of pump and signal losses because, in practice, the waveguides could exhibit some inherent losses due to fabrication imperfections or residual interaction with the analyte substance.

The general signal intensity expression given by Eq. (C2) can account for the pump and signal losses in addition to the idler loss. Using this expression, we display the behavior of signal intensity for different pump and signal loss values in Fig. 7. In the different cases discussed here the magnitude of idler loss is kept fixed at the value $\beta_i'' L = 2.0$, which is the same as the idler loss value used in Fig. 3(b) for the lossy idler case. Therefore, the signal intensity fringes shown by the red solid curves in Figs. 7(a) and 7(b) are essentially the same fringe that we included in Fig. 3(b) in the main text for lossless signal and pump modes. They serve as the reference for the discussion presented here. Signal fringes shown by the green dash-dotted and blue dotted curves in Fig. 7(a) are calculated assuming lossy signal with loss magnitudes $\beta_s'' L = 0.5$ and $\beta_s'' L = 2.0$, respectively. The pump is assumed to be lossless in both these cases. The black dashed fringe in the plot results when both the pump and signal become lossy ($\beta_p'' L = \beta_s'' L = 1.0$). Clearly, the overall signal intensity decreases when signal and pump modes become increasingly lossy. However, it is interesting to note the behavior of signal fringe visibility in these cases. To make this explicit we display the signal intensity spectrum corresponding to lossy signal and pump modes in Fig. 7(b) after rescaling them such that their peak intensity values become equal to that of the lossless (signal and pump) case. Remarkably, we find that the visibility of signal fringes does not suffer much as

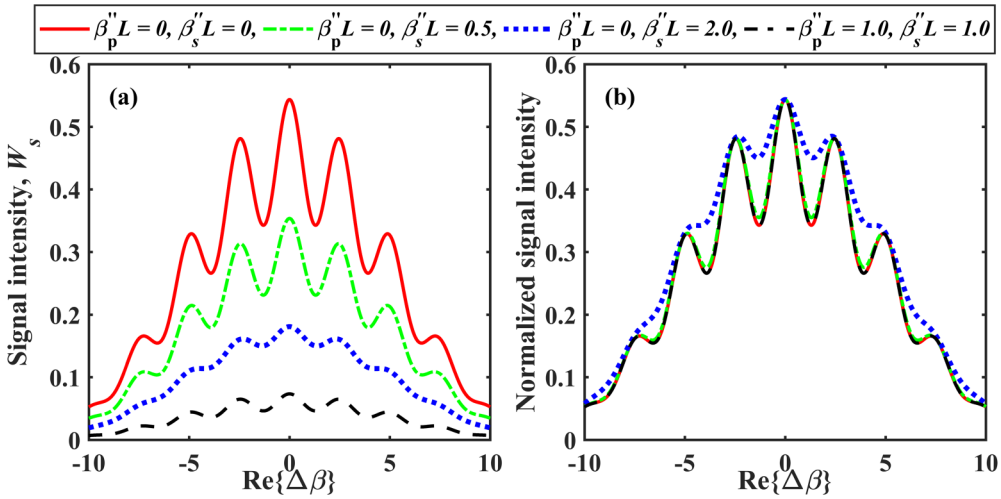

FIG. 7. (a) Signal intensity fringes in the presence of pump and signal losses. These losses are taken as constant over the whole signal spectrum; that is, their dispersive nature is ignored here. Idler loss is taken to be $\beta_i''L = 2.0$ for all four cases shown. (b) Rescaled versions of the signal fringes shown in (a) reflect that the visibility of the fringes does not decrease substantially for moderate pump and signal losses.

long as pump and signal losses remain moderate [see the green dash-dotted spectrum in Fig. 7(b) for an example]. The fringe visibility does reduce substantially, as indicated by the blue dotted curve when the signal or pump losses become large. A case of particular interest arises when the pump and signal losses become equal, $\beta_p''L = \beta_s''L$. This situation is depicted by the black dashed spectrum in Fig. 7(b). Here, even though the overall signal intensity is low, the interference visibility in the signal spectrum is the same as that in the case of a lossless pump and signal (red solid curve). This characteristic behavior of the signal fringe visibility can be attributed to the fact that when $\beta_p'' = \beta_s''$, absorption of pump photons (or generated signal photons) along the waveguide does not add any additional distinguishing information about the position of photon pair creation within the waveguide. As a consequence, balanced pump and signal losses leave the visibility of the signal intensity fringes unaffected, and it is determined only by the idler loss. Mathematically, this effect can be understood by examining the complex phase mismatch parameters $p = \beta_p - \beta_s - \beta_i^* - K$ and $q = \beta_p^* - \beta_s^* - \beta_i^* - K$ used in the signal intensity expression in Eq. (C2). We can clearly see that pump and signal complex propagation constants counter each other in p and q both.

In summary, signal and pump losses can limit the lengths of the waveguides for IC spectroscopy because the absolute signal intensity decreases due to these losses. However, the induced coherence and therefore the resulting fringe visibility do not diminish dramatically for moderate pump and signal losses. Furthermore, we discover a loss-matching condition for pump and signal modes, $\beta_p'' = \beta_s''$, under which the visibility of the signal photon spectral fringe is exclusively controlled by the idler loss. We note that the authors of [41,42] reported a similar loss-matching condition, $\beta_p'' = \beta_s'' + \beta_i''$, in pair generation through SPDC but for the biphoton spectral correlations. The loss-matching condition we find here results in signal photon spectral intensity fringes whose visibility is unaffected by signal and pump losses.

[1] X. Y. Zou, L. J. Wang, and L. Mandel, Induced Coherence and Indistinguishability in Optical Interference, Phys. Rev. Lett. **67**, 318 (1991).

[2] L. J. Wang, X. Y. Zou, and L. Mandel, Induced coherence without induced emission, Phys. Rev. A **44**, 4614 (1991).

[3] M. V. Chekhova and Z. Y. Ou, Nonlinear interferometers in quantum optics, Adv. Opt. Photon. **8**, 104 (2016).

[4] G. B. Lemos, V. Borish, G. D. Cole, S. Ramelow, R. Lapkiewicz, and A. Zeilinger, Quantum imaging with undetected photons, Nature (London) **512**, 409 (2014).

[5] A. Burlakov, Y. B. Mamaeva, A. Penin, and M. Chekhova, Three-wave interference with participation of polaritons, J. Exp. Theor. Phys. **93**, 55 (2001).

[6] D. A. Kalashnikov, A. V. Paterova, S. P. Kulik, and L. A. Krivitsky, Infrared spectroscopy with visible light, Nat. Photon. **10**, 98 (2016).

[7] A. Paterova, S. Lung, D. A. Kalashnikov, and L. A. Krivitsky, Nonlinear infrared spectroscopy free from spectral selection, Sci. Rep. **7**, 42608 (2017).

[8] A. Paterova, H. Yang, C. An, D. A. Kalashnikov, and L. A. Krivitsky, Tunable optical coherence tomography in the infrared range using visible photons, Quantum Sci. Technol **3**, 025008 (2018).

[9] A. V. Paterova and L. A. Krivitsky, Nonlinear interference in crystal superlattices, Light Sci. Appl. **9**, 82 (2020).

[10] K. Kuznetsov, S. Kovalev, G. K. Kitaeva, T. Wang, Y. Lin, Y. Huang, I. Naumova, and A. Penin, Dispersion of the dielectric function real part for Mg :$LiNbO_3$ crystals at terahertz frequencies, Appl. Phys. B **101**, 811 (2010).

[11] G. K. Kitaeva, S. Kovalev, A. Penin, A. Tuchak, and P. Yakunin, A method of calibration of terahertz wave brightness under nonlinear-optical detection, J. Infrared, Millimeter, Terahertz Waves **32**, 1144 (2011).

[12] A. Vanselow, P. Kaufmann, I. Zorin, B. Heise, H. Chrzanowski, and S. Ramelow, Mid-infrared frequency-domain optical coherence tomography with undetected photons, in *Quantum Information and Measurement (QIM) V: Quantum Technologies* (Optical Society of America, Washington, DC, 2019), p. T5A.86.

[13] P.-A. Moreau, E. Toninelli, T. Gregory, and M. J. Padgett, Imaging with quantum states of light, Nat. Rev. Phys. **1**, 367 (2019).

[14] M. Gilaberte Basset, F. Setzpfandt, F. Steinlechner, E. Beckert, T. Pertsch, and M. Gräfe, Perspectives for applications of quantum imaging, Laser Photon. Rev. **13**, 1900097 (2019).

[15] T. P. Grayson and G. A. Barbosa, Spatial properties of spontaneous parametric down-conversion and their effect on induced coherence without induced emission, Phys. Rev. A **49**, 2948 (1994).

[16] M. Lahiri, R. Lapkiewicz, G. B. Lemos, and A. Zeilinger, Theory of quantum imaging with undetected photons, Phys. Rev. A **92**, 013832 (2015).

[17] M. Ravaro, E. Guillotel, M. Le Dû, C. Manquest, X. Marcadet, S. Ducci, V. Berger, and G. Leo, Nonlinear measurement of mid-infrared absorption in AlO_x waveguides, Appl. Phys. Lett. **92**, 151111 (2008).

[18] A. S. Solntsev, P. Kumar, T. Pertsch, A. A. Sukhorukov, and F. Setzpfandt, $LiNbO_3$ waveguides for integrated SPDC spectroscopy, APL Photon. **3**, 021301 (2018).

[19] A. E. Siegman, Lasers without photons—or should it be lasers with too many photons? Appl. Phys. B **60**, 247 (1995).

[20] T. Gruner and D. G. Welsch, Green-function approach to the radiation-field quantization for homogeneous and inhomogeneous Kramers-Kronig dielectrics, Phys. Rev. A **53**, 1818 (1996).

[21] A. N. Poddubny, I. V. Iorsh, and A. A. Sukhorukov, Generation of Photon-Plasmon Quantum States in Nonlinear Hyperbolic Metamaterials, Phys. Rev. Lett. **117**, 123901 (2016).

[22] S. Saravi, A. N. Poddubny, T. Pertsch, F. Setzpfandt, and A. A. Sukhorukov, Atom-mediated spontaneous parametric down-conversion in periodic waveguides, Opt. Lett. **42**, 4724 (2017).

[23] G. Marino, A. S. Solntsev, L. Xu, V. F. Gili, L. Carletti, A. N. Poddubny, M. Rahmani, D. A. Smirnova, H. Chen, A. Lemaître *et al.*, Spontaneous photon-pair generation from a dielectric nanoantenna, Optica **6**, 1416 (2019).

[24] A. Cazé, R. Pierrat, and R. Carminati, Spatial Coherence in Complex Photonic and Plasmonic Systems, Phys. Rev. Lett. **110**, 063903 (2013).

[25] J. E. Sharping, K. F. Lee, M. A. Foster, A. C. Turner, B. S. Schmidt, M. Lipson, A. L. Gaeta, and P. Kumar, Generation of correlated photons in nanoscale silicon waveguides, Opt. Express **14**, 12388 (2006).

[26] M. Fiorentino, S. M. Spillane, R. G. Beausoleil, T. D. Roberts, P. Battle, and M. W. Munro, Spontaneous parametric down-conversion in periodically poled KTP waveguides and bulk crystals, Opt. Express **15**, 7479 (2007).

[27] C. Xiong, C. Monat, A. S. Clark, C. Grillet, G. D. Marshall, M. Steel, J. Li, L. O'Faolain, T. F. Krauss, J. G. Rarity *et al.*, Slow-light enhanced correlated photon pair generation in a silicon photonic crystal waveguide, Opt. Lett. **36**, 3413 (2011).

[28] L. G. Helt, A. M. Brańczyk, M. Liscidini, and M. J. Steel, Parasitic Photon-Pair Suppression via Photonic Stop-Band Engineering, Phys. Rev. Lett. **118**, 073603 (2017).

[29] S. Saravi, T. Pertsch, and F. Setzpfandt, Generation of Counter-propagating Path-Entangled Photon Pairs in a Single Periodic Waveguide, Phys. Rev. Lett. **118**, 183603 (2017).

[30] S. Saravi, T. Pertsch, and F. Setzpfandt, Photonic crystal waveguides as sources of counterpropagating factorizable biphoton states, Opt. Lett. **44**, 69 (2019).

[31] T. Suhara, G. Nakaya, J. Kawashima, and M. Fujimura, Quasi-phase-matched waveguide devices for generation of postselection-free polarization-entangled twin photons, IEEE Photon. Technol. Lett. **21**, 1096 (2009).

[32] H. Herrmann, X. Yang, A. Thomas, A. Poppe, W. Sohler, and C. Silberhorn, Post-selection free, integrated optical source of non-degenerate, polarization entangled photon pairs, Opt. Express **21**, 27981 (2013).

[33] T. Ono, G. F. Sinclair, D. Bonneau, M. G. Thompson, J. C. Matthews, and J. G. Rarity, Observation of nonlinear interference on a silicon photonic chip, Opt. Lett. **44**, 1277 (2019).

[34] M. C. Estevez, M. Alvarez, and L. M. Lechuga, Integrated optical devices for laboratory-on-a-chip biosensing applications, Laser Photon. Rev. **6**, 463 (2012).

[35] W. Lai, S. Chakravarty, X. Wang, C. Lin, and R. T. Chen, On-chip methane sensing by near-IR absorption signatures in a photonic crystal slot waveguide, Opt. Lett. **36**, 984 (2011).

[36] E. Ryckeboer, R. Bockstaele, M. Vanslembrouck, and R. Baets, Glucose sensing by waveguide-based absorption spectroscopy on a silicon chip, Biomed. Opt. Express **5**, 1636 (2014).

[37] Z. Han, P. Lin, V. Singh, L. Kimerling, J. Hu, K. Richardson, A. Agarwal, and D. T. H. Tan, On-chip mid-infrared gas detection using chalcogenide glass waveguide, Appl. Phys. Lett. **108**, 141106 (2016).

[38] L. Tombez, E. J. Zhang, J. S. Orcutt, S. Kamlapurkar, and W. M. J. Green, Methane absorption spectroscopy on a silicon photonic chip, Optica **4**, 1322 (2017).

[39] A. Nitkowski, L. Chen, and M. Lipson, Cavity-enhanced on-chip absorption spectroscopy using microring resonators, Opt. Express **16**, 11930 (2008).

[40] R. Geiss, S. Saravi, A. Sergeyev, S. Diziain, F. Setzpfandt, F. Schrempel, R. Grange, E. B. Kley, A. Tunnermann, and T. Pertsch, Fabrication of nanoscale lithium niobate waveguides for second-harmonic generation, Opt. Lett. **40**, 2715 (2015).

[41] D. A. Antonosyan, A. S. Solntsev, and A. A. Sukhorukov, Effect of loss on photon-pair generation in nonlinear waveguide arrays, Phys. Rev. A **90**, 043845 (2014).

[42] L. G. Helt, M. J. Steel, and J. E. Sipe, Spontaneous parametric downconversion in waveguides: What's loss got to do with it?, New J. Phys. **17**, 013055 (2015).

[43] C. Wang, X. Xiong, N. Andrade, V. Venkataraman, X. F. Ren, G. C. Guo, and M. Loncar, Second harmonic generation in nano-structured thin-film lithium niobate waveguides, Opt. Express **25**, 6963 (2017).

[44] C. Wang, C. Langrock, A. Marandi, M. Jankowski, M. Zhang, B. Desiatov, M. M. Fejer, and M. Loncar, Ultrahigh-efficiency wavelength conversion in nanophotonic periodically poled lithium niobate waveguides, Optica **5**, 1438 (2018).